*Advanced Functional Materials*

ADVANCED FUNCTIONAL MATERIALS
www.afm-journal.de

RESEARCH ARTICLE

# Cu Single Atom Stabilized Au Nanoclusters on $TiO_2$ for Efficient Hydrogen Production

Wen Zhang[1] | Yu Zhou[1] | Xinhao Sun[1] | Shuo Chen[1] | Qinxue Nie[2] | Yangyang Li[1] | Weixin Huang[2] | Seda Karaboğa[3,4] | Emrah Ozensoy[3,5] | Baoqi Yin[1] | Yuanxu Liu[1]

[1]Anhui Province Key Laboratory of Pharmaceutical Preparation Technology and Application, and School of Pharmacy, Anhui University of Chinese Medicine, Hefei, P. R. China | [2]Department of Chemical Physics, University of Science and Technology of China, Hefei, P. R. China | [3]Department of Chemistry, Bilkent University, Ankara, Turkiye | [4]Department of Chemistry, Bolu Abant İzzet Baysal University, Bolu, Turkiye | [5]UNAM National Nanotechnology Center, Bilkent University, Ankara, Turkiye

**Correspondence:** Baoqi Yin (yinbaoqi@ahtcm.edu.cn) | Yuanxu Liu (yuanxliu@ustc.edu.cn)

**Received:** 10 November 2025 | **Revised:** 19 January 2026 | **Accepted:** 3 February 2026

**Keywords:** Au nanoclusters | Cu single atoms | hydrogen production | interfacial interaction

## ABSTRACT

Metal nanoclusters (NCs) with atomically precise structures are widely used for light energy conversion in photocatalysis. However, the challenges in utilizing the photogenerated charges and light-induced photocatalyst instability often result in poor photocatalytic performance. Herein, we investigate tailoring of the local photocatalyst environment and promotion of the charge carrier transfer to increase the reactivity and stability of $Au_n$/Cu-$TiO_2$ photocatalyst in photocatalytic hydrogen evolution from water under UVA illumination via in situ characterizations and theoretical calculations. The interfacial interaction between Au NCs and $TiO_2$ is regulated by precisely-anchored Cu single atoms (SAs) acting as electron acceptors, which can facilitate electron transfer from $TiO_2$ domains to Au NCs, thereby increasing the electron density of Au NCs, expedite electron capture, and enhance hydrogen production efficiency. As a result, $Au_n$/Cu-$TiO_2$ exhibits 16.67 mmol·$g^{-1}$·$h^{-1}$ $H_2$ production rate, 22.7% apparent quantum yield, excellent photocatalytic stability, and recyclability under UVA light irradiation. This work offers novel insights into the rational design of semiconductor photocatalysts promoted with metal NCs and SAs, highlighting the cooperation effect in high photocatalytic performance.

## 1 | Introduction

The production of hydrogen through solar-driven water splitting is widely recognized as a promising and sustainable route for the future clean energy conversion [1–3]. Among the various photocatalytic materials, titanium dioxide ($TiO_2$) has garnered considerable attention [4] and is still regarded as a benchmark photocatalyst for water splitting applications [5]. Despite the advantages of $TiO_2$, it faces notable challenges, including rapid recombination of photogenerated charge carriers and sluggish kinetics associated with proton reduction [6]. Overcoming these limitations is essential to achieving efficient charge separation and maximizing hydrogen production performance. To address these issues, a range of photocatalyst modification strategies have been explored, such as nitrogen-doped-carbon anchored $Fe_3O_4$ nanoparticles offered a sustainable route for industrial oxidant production [7], constructing UCN@PDI catalyst with effective in-electric-filed for photocatalytic $H_2$ production coupled with to high-value carbonyl compounds evolution, avoiding the safety issues and improving atom economy [8], formation of hetero-junctions, and morphological engineering [9]. Among these, the deposition of metal sites onto the $TiO_2$ surface has proven to be particularly effective. This approach enhances charge separation by forming metal-semiconductor Schottky junctions, which

not only facilitate the extraction of photogenerated electrons but also significantly reduce the activation energy required for proton reduction, thereby improving overall photocatalytic performance [10].

In recent decades, catalytic Au nanostructures with diameters smaller than 5 nm have attracted great interest due to their extraordinary catalytic properties [11, 12]. Numerous synthetic strategies were investigated to regulate the size and morphology of small Au particles [13–15]. Recently, atomically precise Au NCs (i.e., Au clusters with well-defined numbers of atoms, shapes, and geometries) have emerged as a novel class of photosensitizers and co-catalysts that are utilized in light energy conversion [16–18], among which hydrogen evolution has received increasing focus as a sustainable means of producing clean fuels [19, 20]. However, the limited structural stability of Au NCs remained a significant challenge for extended photocatalytic performance. Accordingly, thiol-ligated nanostructures were employed to stabilize the Au NCs [21]. Nevertheless, it was observed that catalytic activity was diminished by the surface-bound thiolate ligands, which imposed steric hindrance and blocked the catalytically active undercoordinated surface atoms [22, 23]. Abbas et al. reported $Au_{25}$ NCs revealing highly efficient light-harvesting ability, but these NCs failed to ensure high-performance power conversion characteristics [24]. Mixed valence state of Au species ($Au^+$ and $Au^0$) was exploited frequently in photocatalytic systems to fine-tune interfacial interactions [25]. However, their inability to efficiently facilitate photogenerated carriers limits their utilization in photocatalytic processes. Interestingly, capping ligand-removal from Au active sites was proposed to be responsible for enhanced photocatalytic efficiency by theoretical calculations and experimental characterization [26]. Chen et al. reported that the catalytically active site in the photocatalytic selective oxidation of amines to imines was exposed Au atoms, which were stripped from protective ligands [27]. However, it was also demonstrated that the removal of the thiolate ligand from Au atoms induced unfavorable agglomeration and sintering of Au sites due to Ostwald ripening. For example, Chen et al. reported the formation of relatively large Au nanoparticles with diameters ranging from 4–8 nm upon ligand removal at 180°C [21]. Long et al. found that the size of Au NCs increased to ~3.4 nm after treatment in $H_2/N_2$ mixture at 290°C for 16 h [28]. Furthermore, Gaur et al. showed that the size of Au NCs increased to $3.90 \pm 0.96$ nm when pretreated at 400°C for 1 h [29]. These reports indicate that removal of ligands from undercoordinated Au NCs without accompanying agglomeration or sintering remains a challenge.

Another factor influencing the photocatalytic activity of metal NCs/semiconductor systems is the physical and chemical properties of the catalytic support material. The NC/semiconductor interaction at the interface is critical, as it plays a significant role in charge redistribution and transportation. Activated carbon materials, metal-organic frameworks, metal oxides with defects, and pyrolyzed graphene oxides have been used as photocatalytic support materials to anchor Au NCs [30–34]. Particularly, the high photocatalytic hydrogen production activity and stability could be achieved on $TiO_2$ [35]. However, $TiO_2$ suffers from high charge carrier recombination rates and slow redox kinetics [36]. Recently, Cu SAs have attracted significant attention due to the maximized atom utilization efficiency [37]. Zhang et al. reported that SA Cu-$TiO_2$ revealed higher $H_2$ generation rates compared with various metals loaded on $TiO_2$ derived from MIL-125 (Ti) [38]. Wang et al. demonstrated that the PtCu-$TiO_2$ photocatalyst could achieve 99.2% apparent quantum efficiency of hydrogen production via the synergy between Cu single atoms and Pt nanodots [39]. Moreover, the transformation of active $Cu^{\delta+}$ into inactive $Cu^0$ may be regulated by adjusting the presence or absence of $O_2$ in the reaction system [40]. Although previous works indicated that the synergistic effect of metal SAs with NCs or NPs could enhance photocatalytic performance, no further insights into the fundamental understanding of the synergistic function of Cu SAs and $Au_{25}$ NCs on $TiO_2$ have been revealed. Therefore, rational surface engineering of $Au_{25}$ NCs deposited on Cu SA-anchored $TiO_2$ appears as a promising approach that can provide mechanistic insights for interpreting the photocatalytic performance of such systems in hydrogen production from water.

In this work, we introduce Cu SAs onto $TiO_2$ catalysts to tune the local environments of $Au_{25}$ NCs, aiming to regulate the coordination and electronic structure. Theoretical calculations and experimental structural characterization measurements demonstrate that Au NCs serve as the active sites in the $Au_n$/Cu-$TiO_2$ photocatalyst architecture, enabling enhanced $H_2$ generation performance upon optimization of the Au NCs electronic structure. By carefully tuning the amount of Au NCs and Cu SAs, the currently reported optimized photocatalyst exhibits an apparent quantum efficiency of 22.7% at room temperature and a $H_2$ generation activity of 16.67 $mmol \cdot g^{-1} \cdot h^{-1}$ under UVA irradiation, corresponding to 59 times greater $H_2$ generation activity than that of pristine $TiO_2$ with $_a$ mixture of anatase and rutile. Most notably, the size of $Au_{25}$ NCs was successfully preserved after high-temperature activation, ligand removal, and illumination steps. The superior activity and the long-term stability of $Au_n$/Cu-$TiO_2$ photocatalyst in photocatalytic hydrogen evolution are attributed to the significantly enhanced electron transfer from $TiO_2$ domains to $Au_{25}$ NCs facilitated by Cu SAs serving as an electronic bridge through strong interfacial interaction.

## 2 | Results and Discussion

### 2.1 | Photocatalyst Fabrication and Structural Characterization

The synthesis process of $Au_n$/Cu-$TiO_2$ photocatalyst was implemented (Figure 1a) via the strong electrostatic interaction and the confinement effect [41]. The Zeta potential test of $NH_2$-MIL-125 indicates a negative potential value in Figure S1, which is compatible with the electrostatic adsorption of $Cu^{2+}$ ions onto the Ti vacancies in $NH_2$-MIL-125; meanwhile, the high specific surface area (1257.1 $m^2\ g^{-1}$) and well-defined porosity (Figure S2a,b), which collectively facilitate the anchoring of Cu ions. Following the incorporation of Cu in $NH_2$-MIL-125, the XRD pattern of the resulting composite is nearly identical to that of the pristine $NH_2$-MIL-125 (Figure S2c), indicating the uniform encapsulation of Cu ions within the framework with excellent dispersity. Through pyrolytic transformation from $NH_2$-MIL-125 into porous $TiO_2$, Cu species undergo in-situ anchoring as Cu-SA sites on porous $TiO_2$, resulting in the fabrication of a Cu-SAs/$TiO_2$ [40]. More importantly, Cu-SAs/$TiO_2$ with a Zeta potential value of +9.6 eV can readily electrostatically adsorb the negatively charged $Au_{25}$ NCs to form $Au_n$/Cu-$TiO_2$ photocatalyst.

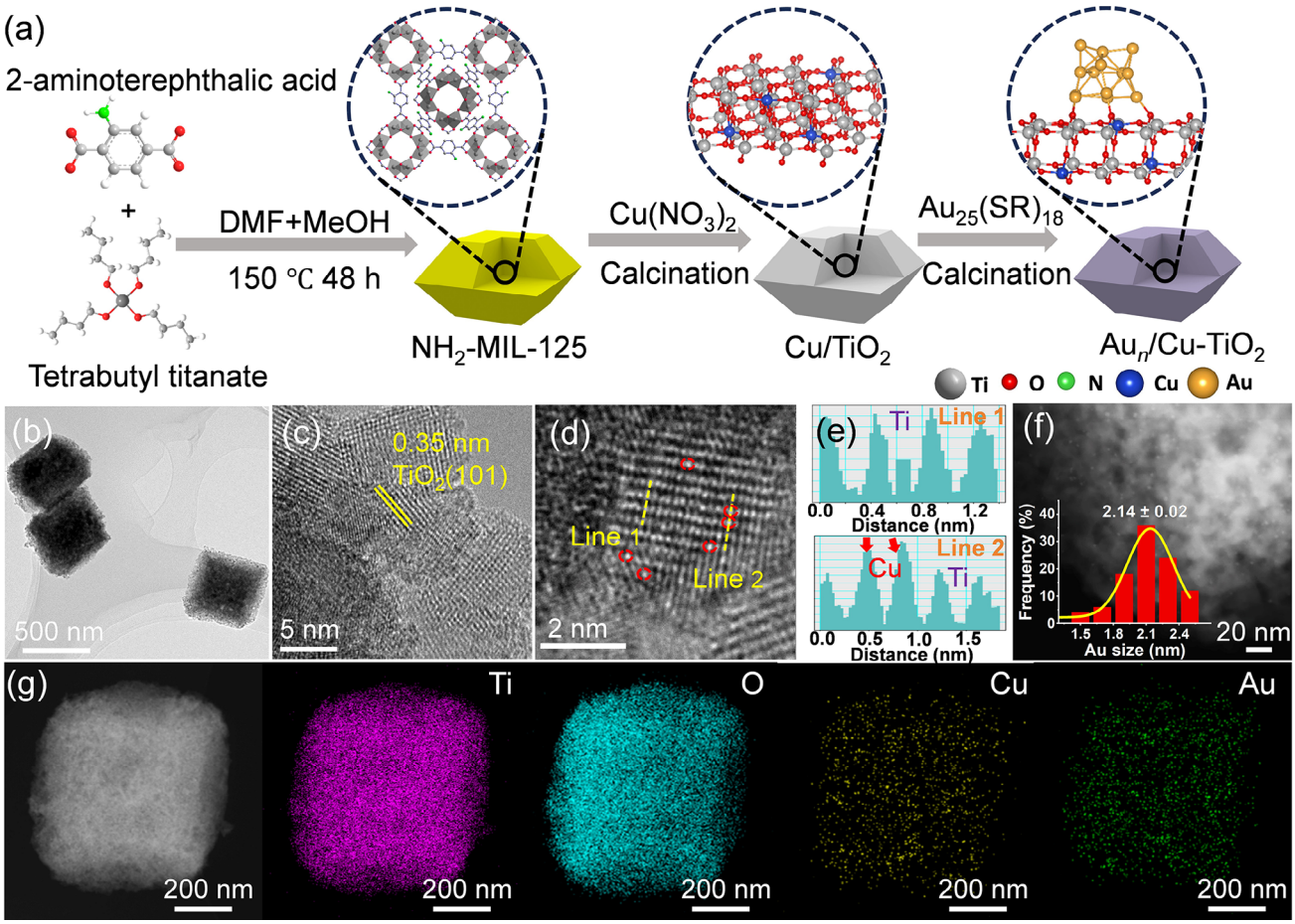


**FIGURE 1** | (a) Schematic diagram of the synthesis process. (b) TEM image. (c, d) High-resolution TEM images. (e) Corresponding atomic intensity distributions of Line 1 and Line 2 marked in panel (d) for $Au_n$/Cu-$TiO_2$. (f) HAADF-STEM image and size distribution of $Au_{25}$ NCs on $Au_n$/Cu-$TiO_2$. (g) Elemental distribution mapping of Ti, O, Cu, and Au on $Au_n$/Cu-$TiO_2$.

TEM, HRTEM, and HAADF-STEM were used to analyze the structure and spatial distribution of Cu SAs and Au NCs on the $TiO_2$. The as-prepared $NH_2$-MIL-125 exhibits a decahedral shape with a particle size of ~700 nm and a smooth surface (Figure S3). The TEM image (Figure 1b) of $Au_n$/Cu-$TiO_2$ maintains the decahedral structural inherited from $NH_2$-MIL-125 but with collapsed morphology and slightly rougher surface due to the high temperature activation. The observed lattice spacing was measured to be 0.35 nm (Figure 1c), which corresponded to the (101) plane of anatase $TiO_2$ crystal structure. Owing to its porous structure and unsaturated bonds, $NH_2$-MIL-125 not only stabilizes the Cu ions but also ensures a single-atom distribution of Cu in the resulting photocatalysts. In light of former studies [42–44], the bright spots marked by red circles from different regions of $Au_n$/Cu-$TiO_2$ were assigned to Cu SAs in the enlarged HAADF-STEM image (Figure 1d; Figure S4), and no Cu or $Cu_xO$ clusters/particles were detected. The randomly selected line scans profiles marked with yellow dashed lines containing both Ti and Cu atoms were shown in Figure 1e, where the Cu atoms lead to higher corrugations than Ti. Additionally, the darker regions and rougher surface suggest a defective structure for the $TiO_2$ support [45], enabling coordinatively unsaturated surface sites which can facilitate chemisorption of $Au_{25}$ NCs. The $Au_{25}$ NCs in the $Au_n$/Cu-$TiO_2$-uc sample displayed a homogeneous and uniform particle size distribution with an average size of 1.3 nm (Figure S5). For ligand removal, the temperature range generally varies between 150°C and 400°C [46]. In the current work, even after employing an extremely high calcination temperature of 400°C, it was observed that $Au_n$/Cu-$TiO_2$ photocatalyst maintained its significantly small average particle size of 2.1 nm (Figure 1f). This finding is in stark contrast with that of $Au_{25}$ NCs over $TiO_2$ or other metal oxide supports, where the agglomeration of $Au_{25}$ was evident after pretreatment at high temperature [47–49]. Along these lines, the average Au particle size on the Au/$TiO_2$ control sample was 4.7 nm (Figure S6), revealing a notably greater Au particle size than that of $Au_n$/Cu-$TiO_2$. These results suggested that the Cu SA-optimized $TiO_2$ can efficiently anchor Au NCs on Cu/$TiO_2$ and boost their resistance toward sintering, thereby facilitating the catalytic activity. The EDX line scans obtained across the white dashed rectangle shown in Figure S7 clearly illustrate that Cu and Au signals positionally overlap along the line scans, indicating that Cu sites or other surface sites within the close proximity of Cu sites on the $Au_n$/Cu-$TiO_2$ surface function as Au anchoring sites. Meanwhile, the STEM-EDS mapping further verifies the homogeneous existence of Cu atoms and Au NCs on $TiO_2$ without agglomeration (Figure 1g).

The Au and Cu contents of $Au_n$/Cu-$TiO_2$ photocatalyst were measured by inductively coupled plasma optical emission spectrometry (ICP-OES), as shown in Table S1, in which the optimal

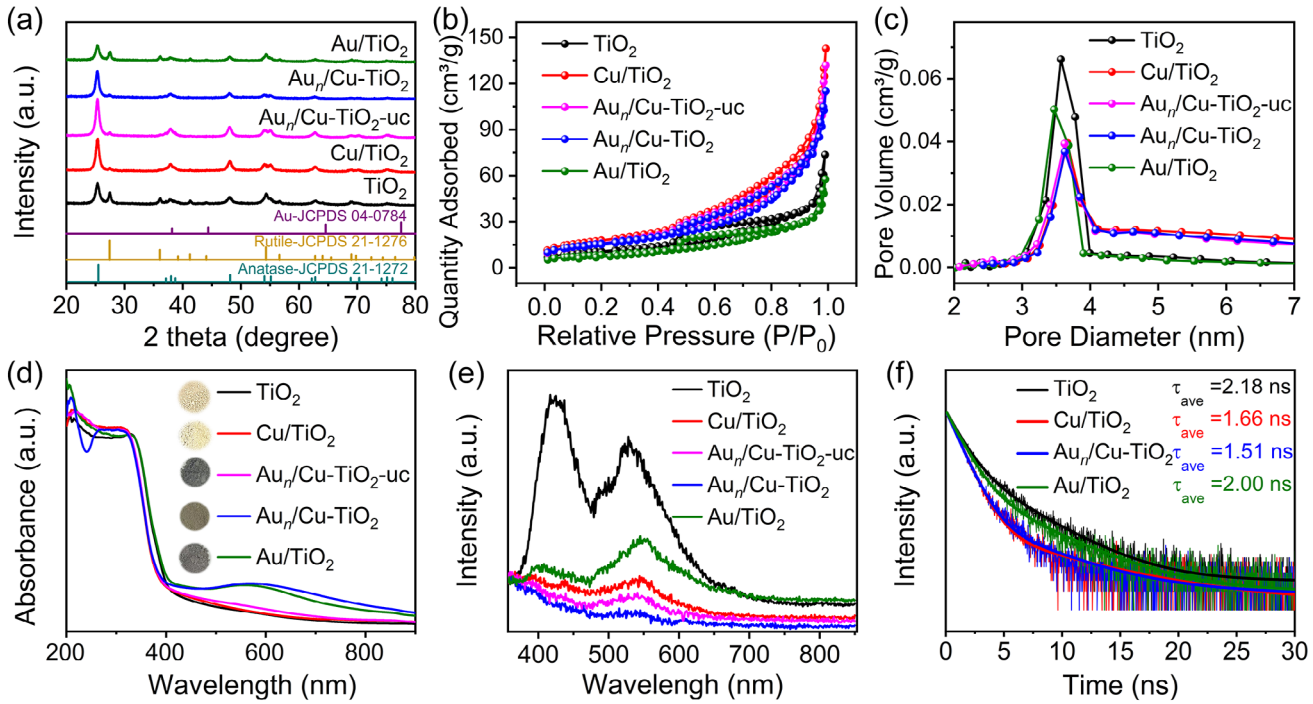


**FIGURE 2** | (a) XRD spectra. (b) $N_2$ adsorption-desorption isotherms. (c) Pore size distributions. (d) UV–vis absorption spectra and optical photographs revealing the colors of the samples. (e) PL spectra. (f) PL decay spectra of photocatalysts.

$Au_n$/Cu-$TiO_2$ photocatalyst has 0.13 wt% Cu and 0.24 wt% Au content. The XRD patterns of samples (Figure 2a) confirmed the presence of $TiO_2$ structure comprised of both anatase and rutile (JCPDS 21–1272 and JCPDS 21–1276, respectively) polymorphs [50], while Cu doped samples exhibited predominantly anatase phase, where rutile existed only as a minority phase. This observation suggests that the introduction of Cu can stabilize the anatase phase and inhibit the anatase to rutile phase transition at $T \leq 400°C$ [51]. For the Au/$TiO_2$ composite, the observed mixed-phase of anatase and rutile exhibits a crystal structure consistent with that of currently prepared pristine $TiO_2$, suggesting that Au NPs are loaded on the surface of $TiO_2$ rather than incorporated into its lattice. No diffraction peaks belonging to Au were detected in any of the investigated samples, consistent with extremely small and quite well-dispersed Au clusters on $TiO_2$.

BET analysis (Figure 2b) showed type IV isotherm curves consistent with a mesoporous structure for all catalysts [52]. It is clear from Figure 2c and Table S2 that the introduction of Cu species appeared to increase the specific surface area, average pore size, and average mesopore volume, which is also probably closely linked to the stability of $Au_{25}$ NCs on the Cu-containing support materials [53].

The optical characteristics were investigated by UV–vis diffuse reflection spectra, as depicted in Figure 2d. The absorption thresholds were analyzed, and corresponding band gap values, along with the band potentials via Mott-Schottky analysis, were listed in Figures S8 and S9 and Table S3 [54–56]. In comparison to pristine $TiO_2$, all Cu doped samples show wider band gaps as opposed to Cu-free counterparts, while adding only Au to $TiO_2$ does not alter the band gap of $TiO_2$. This suggests that Cu species interacted strongly with the $TiO_2$ lattice for Cu/$TiO_2$, $Au_n$/Cu-$TiO_2$-uc, and $Au_n$/Cu-$TiO_2$, resulting in a significant alteration in the $TiO_2$ bulk electronic structure, evident by the increasing bandgap, while Au supported on $TiO_2$ in the absence of Cu only led to a minor change in the electronic bandgap of $TiO_2$ [57]. Notably, the appearance of broad absorption bands at 400–600 nm and 600–800 nm in Cu/$TiO_2$, $Au_n$/Cu-$TiO_2$-uc, and $Au_n$/Cu-$TiO_2$ can be attributed to the charge transfer from $TiO_2$ to $Cu^{\delta+}$ and d–d transition of $Cu^{2+}$ sites [5, 58]. Besides, $Au_n$/Cu-$TiO_2$ exhibits an asymmetric peak at 560 nm rather than a surface plasmonic resonance (SPR) peak characteristic of Au nanoparticles, confirming that $Au_{25}$ NCs maintain their small size on the Cu/$TiO_2$ surface [19]. In contrast, the Au/$TiO_2$ photocatalyst exhibits a distinct absorption center and intensity related to the particular size of Au clusters and their distinct electronic structure. These results are consistent with the corresponding color changes of the samples depicted in Figure 2d, as darker samples exhibited higher absorbance in the visible light region. Based on the current results, we propose that under light irradiation, incorporation of trace amounts of Cu SAs in $TiO_2$ leads to alteration of the electronic properties of $TiO_2$ and enrichment of the electron density of Au NCs.

The extent of separation of photogenerated charge carriers by the samples was further examined by PL spectra, as shown in Figure 2e. $TiO_2$ shows strong emission signals at 423 and 530 nm, which can be attributed to the radiative recombination of trapped exciton states at the lattice imperfections and shallow traps on vacancies or defects, respectively [59]. The diminished steady-state PL peak of $Au_n$/Cu-$TiO_2$ suggested efficient charge migration and charge separation as a result of the presence of Cu SAs. Additionally, the shortest average fluorescence lifetime of $Au_n$/Cu-$TiO_2$ from the PL decay tests ($\lambda_{ex} = 360$ nm, $\lambda_{em} = 475$ nm) also supported the increased rate of migration of charge carriers

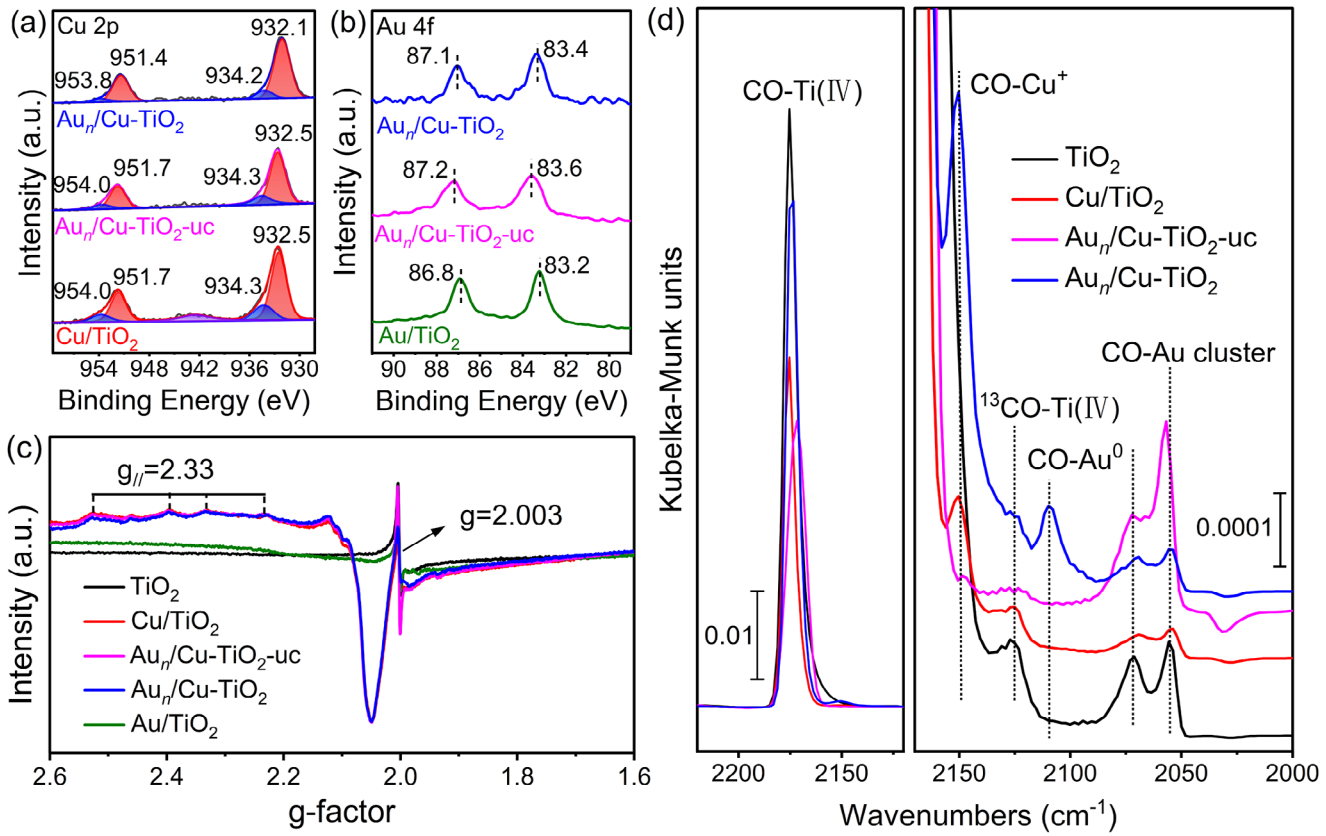


**FIGURE 3** | (a) XPS spectra of Cu 2p. (b) XPS spectra of Au 4f. (c) Low temperature EPR spectra. (d) In situ DRIFTS spectra of CO adsorption at 123 K and $P_{CO}$ = 100 Pa.

from the bulk to the interface (Figure 2f; Table S4), which further promoted the activity of $H_2$ production of the photocatalyst.

Ti 2p XPS measurements of all photocatalysts (Figure S10) reveal two major peaks at 458.6–458.8 eV and 464.2–464.4 eV corresponding to Ti $2p_{3/2}$ and Ti $2p_{1/2}$ features of $Ti^{4+}$ states on the surface, respectively [60]. The O 1s spectra (Figure S11) can be deconvoluted into three peaks that can be assigned to lattice oxide ($O_L$) at 529.9–530.1 eV, defective oxide ($O_V$) at 531.5–531.7 eV, and hydroxide or $H_2O$ groups ($O_H$) at 532.5–532.7 eV, respectively [61]. The main Cu 2p features of Cu/$TiO_2$ and Au$_n$/Cu-$TiO_2$-uc located at 932.5 eV and 951.7 eV correspond to Cu $2p_{3/2}$ and Cu $2p_{1/2}$ signals of $Cu^+$ and (or) $Cu^0$ species, respectively, where 934.3 eV and 954.0 eV are assigned to the Cu $2p_{3/2}$ and Cu $2p_{1/2}$ of $Cu^{2+}$ (Figure 3a), the weak intensity of characteristic shake-up satellite peaks in the range of 940–945 eV suggests that small fraction of surface $Cu^{2+}$ may exist in our samples [62]. However, the binding energy is negatively shifted to 932.1 and 951.4 eV in Au$_n$/Cu-$TiO_2$ with calcination, suggesting the transfer of electrons from $TiO_2$ to Cu due to the strong interaction. The Au 4f spectrum of $Au_{25}$ NCs is shown in Figure S12. The Au $4f_{7/2}$ peak was observed at 84.4 eV, which is consistent with the value observed for pure $Au_{25}$ NCs [63]. For Au$_n$/Cu-$TiO_2$-uc (Figure 3b), the binding energy of Au $4f_{7/2}$ appears at 83.6 eV, revealing a significant negative shift. As expected, the Au $4f_{7/2}$ peak for Au$_n$/Cu-$TiO_2$ is located at 83.4 eV, which is consistent with a negative shift compared to that of Au$_n$/Cu-$TiO_2$-uc originating from the cleavage of Au—S bonds after calcination at 400°C, in good agreement with a previous report [64]. However, the measured Au $4f_{7/2}$ binding energy for Au/$TiO_2$ is 83.2 eV, illustrating a negative shift after calcination. This shift can be attributed to the agglomeration of gold species during the ligand removal via calcination, which resulted in the enlargement of Au clusters.

The low-temperature EPR data of the currently synthesized $TiO_2$ (Figure 3c) exhibit an intense signal at g = 2.003 associated with the oxygen vacancies in $TiO_2$ [65], which was also reported in former studies [50]. On the other hand, Cu containing samples show a clearly discernible hyperfine structure with g// = 2.33, corresponding to the $Cu^{2+}$ ions in the bulk [66], which further indicates that the Cu SAs were anchored successfully in Au$_n$/Cu-$TiO_2$. Generally, $Ti^{3+}$ will be formed from the excess electrons generated by oxygen vacancies [67]. However, in the presence of Au NCs, the excess electrons from oxygen vacancies presumably transfer to Au instead of the neighboring Ti.

To further investigate the structure and surface compositions of the catalysts, we analyzed all the samples using CO adsorption at 123 K via in situ DRIFTS. As shown in Figure 3d, for all investigated samples, a strong vibrational feature at 2175 $cm^{-1}$ and a minor vibrational feature at around 2125 $cm^{-1}$ are observed, which arise from CO and $^{13}CO$ adsorbed at 5-coordinated Ti sites on $TiO_2$, respectively [68]. On the other hand, two additional vibrational features located at 2072 $cm^{-1}$ and 2055 $cm^{-1}$ for pristine $TiO_2$ can be assigned to CO adsorption on surface defect sites of $TiO_2$ (i.e., oxygen vacancies with different local environments). For the Cu/$TiO_2$ surface, besides the similar vibrational features with $TiO_2$, a new vibrational signal at

2149 $cm^{-1}$ is visible that could be related to CO coordinated to $Cu^{+}$ sites [69]. While incorporating only Cu into $TiO_2$ (i.e., for $Cu/TiO_2$) does not alter the IR intensity ratio of 2072 $cm^{-1}$ and 2055 $cm^{-1}$ signals in a significant manner, addition of Au to the $Cu/TiO_2$ structure to form $Au_n/Cu\text{-}TiO_2$-uc significantly boosts the relative intensity of the IR feature at 2055 $cm^{-1}$ which can be explained by CO adsorption on Au NCs present on the $Au_n/Cu\text{-}TiO_2$-uc surface. It can be seen that upon calcination of the $Au_n/Cu/TiO_2$-uc sample (i.e., on $Au_n/Cu\text{-}TiO_2$), relative intensity of the IR signal at 2055 $cm^{-1}$ decreases, while a new IR feature appears at 2109 $cm^{-1}$ attributed to CO adsorption on $Au^0$ sites whose formation indicates the successful removal of the strong electron-donated thiolate ligands [70]. Furthermore, the negative shift in the Au 4f peak following ligand removal also corroborates this conclusion (Figure 3b).

## 2.2 | Photocatalyst Performances

The photocatalytic performances of $TiO_2$ and $Cu/TiO_2$ photocatalysts promoted with different Cu contents (Figure S13) have been evaluated for photocatalytic hydrogen production under UVA irradiation. Compared to the MOF-derived $TiO_2$, the introduction of Cu SAs improved the photocatalytic activity, which can be attributed to the fast electron transfer from $Cu^{2+}$ to $Cu^{+}$ sites [38, 71]. Notably, $0.5\%Cu/TiO_2$ photocatalyst exhibited the best photocatalytic hydrogen production activity among other $Cu/TiO_2$ photocatalysts over the entire measured time, yielding an average hydrogen production rate of 4.24 $mmol{\cdot}g^{-1}{\cdot}h^{-1}$, which is approximately 15 times higher than that of pristine $TiO_2$. Furthermore, the UV–vis diffuse reflectance spectrum of $Cu/TiO_2$ (Figure S14) revealed a slight improvement in visible light absorption in the range of 400–800 nm. To investigate the synergistic function of Au NCs and Cu SAs on $TiO_2$ in the enhancement of photocatalytic $H_2$ production, the photocatalytic performances of different samples were compared (Figure 4a). Clearly, the photocatalytic activities are significantly enhanced by loading Au NCs on Cu SAs as expected, which may be caused by the tuned local environment of Cu SAs attributed to the rapid charge transfer in $Au_n/Cu\text{-}TiO_2$ [72]. The activity of $Au_n/Cu\text{-}TiO_2$ is higher than that of $Au_n/Cu\text{-}TiO_2$-uc, which may be due to the removal of ligands exposing a large number of Au species, providing a larger number of catalytically active sites for the reaction. In contrast, the photocatalytic activity of $Cu/TiO_2$ is slightly better than that of $Au/TiO_2$, which may be due to the abundance of Cu SAs acting as charge transfer centers. Furthermore, the improvement in the hydrogen production activity is more remarkable for the $0.5\%Au_n/Cu\text{-}TiO_2$ catalyst. Interestingly, upon further increasing Au content, the $H_2$ evolution performances decreased significantly, as shown in Figure S15. This may result from the agglomeration of Au on the $TiO_2$ surface at high Au loadings (Figures S16 and S17). The average $H_2$ evolution rates were also measured for the investigated photocatalysts under UVA irradiation for 4 h, resulting in the following order of photocatalytic reactivity: $Au_n/Cu\text{-}TiO_2 > Au_n/Cu\text{-}TiO_2$-uc $> Cu/TiO_2 > Au/TiO_2 > TiO_2$ (Figure 4b). The $H_2$ evolution rate of $Au_n/Cu\text{-}TiO_2$ is 16.67 $mmol{\cdot}g^{-1}{\cdot}h^{-1}$, which is nearly 2 times, 4 times, 5 times and 60 times superior than that of $Au_n/Cu\text{-}TiO_2$-uc (8.01 $mmol{\cdot}g^{-1}{\cdot}h^{-1}$), $Cu/TiO_2$ (4.24 $mmol{\cdot}g^{-1}{\cdot}h^{-1}$), $Au/TiO_2$ (3.27 $mmol{\cdot}g^{-1}{\cdot}h^{-1}$) and $TiO_2$ (0.28 $mmol{\cdot}g^{-1}{\cdot}h^{-1}$, respectively. Subsequently, the apparent quantum yield (AQY) of the $0.5\%Au_n/Cu\text{-}TiO_2$ catalyst for $H_2$ evolution under monochromatic light irradiation at different wavelengths ($\lambda$ = 365 nm, 380 nm, 400 nm, 420 nm, and 450 nm) was measured (Figure 4c), which aligned well with the light absorption profile. Notably, an AQY of 22.7% at 365 nm was achieved for sacrificial $H_2$ production. In comparison with previously reported Cu and/or Au modified $TiO_2$ photocatalysts, $0.5\%Au_n/Cu\text{-}TiO_2$ exhibits outstanding $H_2$ evolution performance (Table S5). Furthermore, compared with the $Au/Cu\text{-}TiO_2$-PD photocatalyst (9.82 $mmol{\cdot}g^{-1}{\cdot}h^{-1}$) revealing an average Au particle size of 11 nm, it is clear that Au NCs on $0.5\%Au_n/Cu\text{-}TiO_2$ exhibit significantly better catalytic performance than Au nanoparticles on $Au/Cu\text{-}TiO_2$-PD (Figure S18).

The recycling stability test of $0.5\%Au_n/Cu\text{-}TiO_2$ shows that the $H_2$ evolution rate over 12 successive cycles for 48 h is stable, demonstrating the excellent stability of this photocatalyst (Figure 4d). Furthermore, after sealed storage for eight months under dark conditions, the photocatalytic performance of $0.5\%Au_n/Cu\text{-}TiO_2$ was found to be comparable to that of the fresh sample (Figure S19), illustrating the exceptional stability of the $Au_n/Cu\text{-}TiO_2$ photocatalyst. We speculate that the strikingly high photocatalytic activity of $Au_n/Cu\text{-}TiO_2$ may result from the rapid transport and separation of photogenerated charge carriers. To further investigate the charge carrier transfer, the transient photocurrent responses were subsequently conducted, and the observed photocurrents are shown in Figure 4e. $Au_n/Cu\text{-}TiO_2$ presents a higher photocurrent than $Cu/TiO_2$, $Au/TiO_2$, and $TiO_2$, indicating more efficient carrier separation. This might be due to the favorable action of copper sites mediating efficient electron transfer to Au NC active sites, where $H_2$ generation takes place. Concurrently, the photocurrent response of $Au_n/Cu\text{-}TiO_2$ also exhibits expected stability and repeatability for several on/off cycles. In addition, the electrochemical impedance spectra (EIS) are also presented in Figure 4f. $Au_n/Cu\text{-}TiO_2$ shows dramatically decreased resistance radius in the EIS Nyquist curve, suggesting rapid electron transport to surface sites for hydrogen reduction reactions.

## 2.3 | Theoretical Calculation

To gain insight into the effect of the doped Cu SAs and supported Au NCs on photocatalytic activity at the molecular level, optimized computational models (Figures S20 and S21) of $Au/TiO_2$ and $Au_n/Cu\text{-}TiO_2$ were constructed based on the experimental results, and comparative analyses were performed using DFT simulations to explore the mechanism of high photocatalytic activity on $Au_n/Cu\text{-}TiO_2$. The adsorption energy ($E_{ads}$) of the Au NCs with $TiO_2$ and $Cu/TiO_2$ was calculated as −4.93 eV and −6.87 eV, respectively (Figure 5a). The higher $E_{ads}$ value of $Au_n/Cu\text{-}TiO_2$ indicates a more stable adsorption configuration for Au NCs on the $Cu/TiO_2$ surface as compared to that of $TiO_2$ [73]. The differential charge density distribution is also illustrated in Figure 5b. A stronger negative charge enrichment is observed for Au NCs on $Au_n/Cu\text{-}TiO_2$ with a Bader charge of −1.36 |e| as compared to −1.16 |e| for $Au/TiO_2$. These results are in good agreement with an enhanced charge transfer from $Cu/TiO_2$ to Au NCs and the formation of a stronger internal electric field at the interface of $Au_n/Cu\text{-}TiO_2$. These observations illustrate that the presence of Cu SAs can effectively facilitate interfacial electron transfer, while the Au NCs act as an

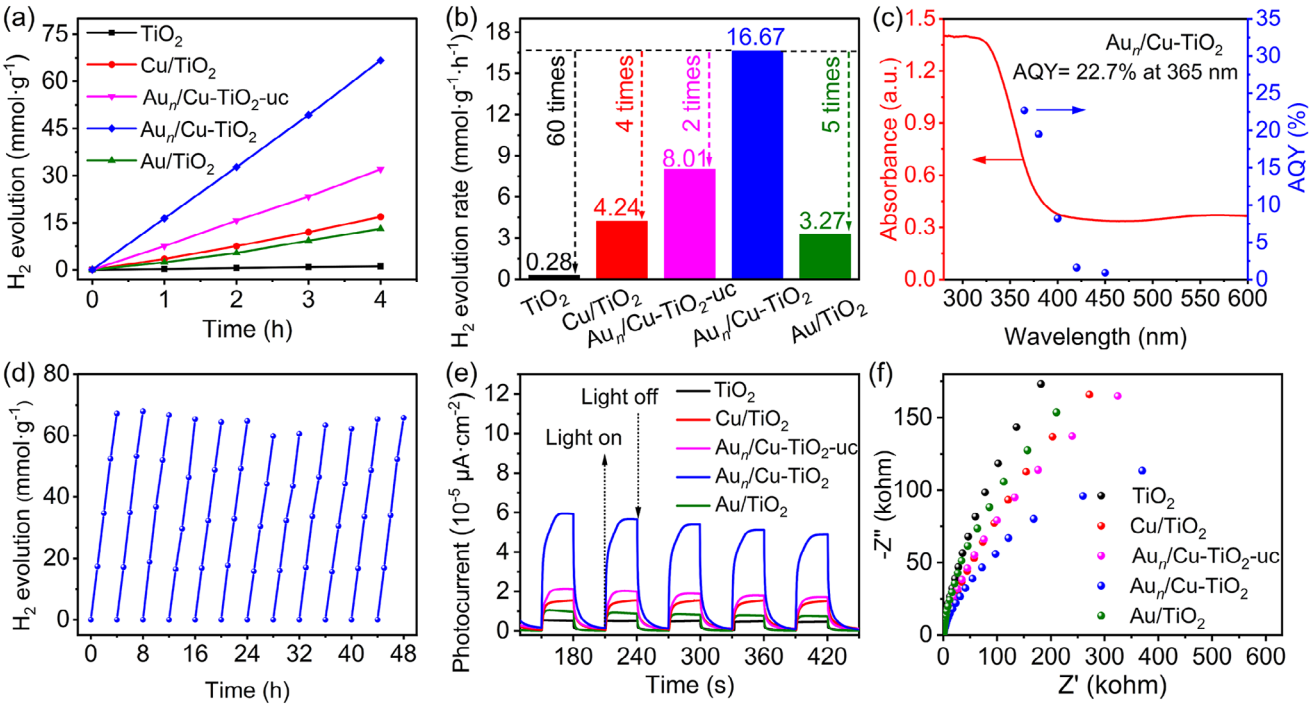


**FIGURE 4** | (a,b) Photocatalytic hydrogen production. (c) The wavelength-dependent AQY of $Au_n$/Cu-$TiO_2$ in photocatalytic hydrogen evolution. (d) Cycling stability of $Au_n$/Cu-$TiO_2$ over 12 successive tests for 48 h. (e) Transient photocurrent response curves of different samples. (f) EIS curves of different samples under LED light.

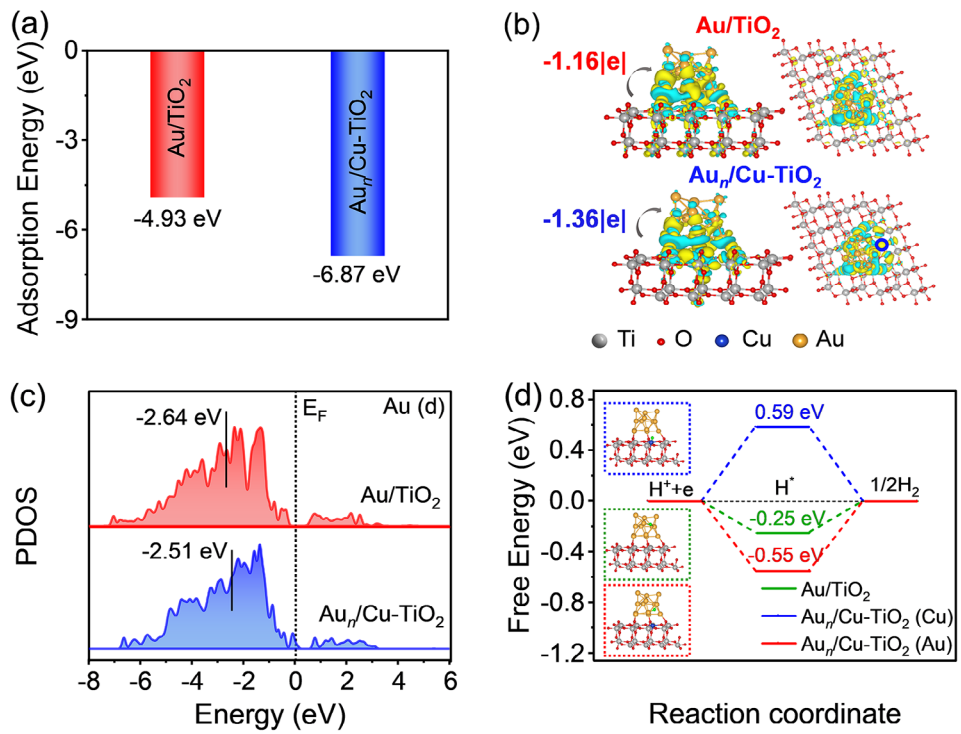


**FIGURE 5** | (a) Adsorption energies of Au NCs on $TiO_2$ and Cu/$TiO_2$. (b) Differential charge density of Au/$TiO_2$ and $Au_n$/Cu-$TiO_2$, where yellow and cyan areas represent electron accumulation and depletion, respectively. (c) PDOS of Au/$TiO_2$ and $Au_n$/Cu-$TiO_2$. (d) Gibbs free energy ($\Delta G_{H^*}$) diagram for photocatalytic hydrogen evolution reactions on Au/$TiO_2$ and $Au_n$/Cu-$TiO_2$ surfaces.

electron sponge, synergistically regulating the interfacial charge distribution through electron storage and thereby enhancing hydrogen production efficiency. This mechanism rationalizes the experimental observation that the incorporation of Cu SAs into the $TiO_2$ support enables the formation of $Au^0$ NCs as the active species. Meanwhile, the doping of Cu SAs into $TiO_2$ promotes the adsorption of reaction intermediates and induces an upshift of the d-band center of Au NCs compared to unmodified $TiO_2$ (Figure 5c) [74]. This has also been confirmed by the calculated Gibbs free energy changes (ΔG) for the adsorption of H* intermediates on $Au_n$/Cu-$TiO_2$ (−0.55 eV), being much lower than that of Au/$TiO_2$ (−0.25 eV) (Figure 5d). Furthermore, a comparison of ΔG values at Au and Cu sites in $Au_n$/Cu-$TiO_2$ revealed that the Au site is more likely to be the active center for catalytic hydrogen evolution due to the lowest hydrogen adsorption energy of Au (−0.55 eV) than Cu (+0.59 eV) [75]. Current computational results indicated that the existence of Cu SAs contributes to the optimization of the photocatalyst electronic structure and enhancement of the $H_2$ generation performance for $Au_n$/Cu-$TiO_2$.

In order to explore the charge carrier dynamics in $Au_n$/Cu-$TiO_2$ during the photocatalytic reaction, the driving force for charge carrier separation and migration over the photocatalyst was probed by measuring the surface charge density and surface photovoltage [76]. Kelvin probe force microscopy (KPFM) measurements of surface charge revealed that under dark conditions, $Au_n$/Cu-$TiO_2$ exhibits a higher surface potential (ΔE = 45.22 mV) than Au/$TiO_2$ (ΔE = 36.11 mV) (Figure 6a), indicating a greater charge density. Upon light illumination, the ΔE value of $Au_n$/Cu-$TiO_2$ increases markedly to 57.11 mV, significantly exceeding that of Au/$TiO_2$ (ΔE = 41.37 mV). These findings confirm that Cu SAs facilitate electron transfer and enhance more efficient charge carrier separation [77]. Consistently, steady-state surface photovoltage spectroscopy (SPV) further elucidates the photo-induced carrier transfer dynamics; a substantially stronger SPV signal is observed for $Au_n$/Cu-$TiO_2$ compared to Au/$TiO_2$ (Figure S22), reflecting its superior efficiency in transporting charges to the surface. XPS spectra are measured to comparatively examine the electronic interaction. As shown in Figure 6b, the Ti 2p peak shifted toward higher binding energy after light irradiation as compared to that of the fresh catalyst. Furthermore, the Au 4f XPS peak shifted towards lower binding energy (Figure 6c), although there was no obvious binding energy shift for the Cu 2p XPS signal (Figure 6d), but the $Cu^{2+}$ on the surface almost disappeared. In parallel, the EPR signal intensity of $Cu^{2+}$ species decreases significantly (Figure 6e). This is probably due to the reduction of some of the $Cu^{2+}$ sites into EPR-silent $Cu^+$ species. These observations point to the existence of electron transfer from $TiO_2$ to $Cu^{2+,}$ followed by electron transport to Au NCs. Thus, for $H_2$ evolution, the enhanced photocatalytic activity is effectively tuned by the doped Cu SAs. As suggested by the currently presented experimental and theoretical results, a reaction mechanism for $H_2$ evolution on $Au_n$/Cu-$TiO_2$ with a small amount of Cu SAs and Au/$TiO_2$ can be proposed as shown in Figure 6f. Upon illumination of $Au_n$/Cu-$TiO_2$, $Cu^{2+}$ SAs act as electron traps to form $Cu^+$ and migrate electrons to Au NCs for the reduction reaction. Compared to Au/$TiO_2$, the regulation of the local environment and electron density gives rise to the superior photocatalytic hydrogen production performance. The XRD, SEM, and TEM results for $Au_n$/Cu-$TiO_2$ were characterized after the cycle stability test and are shown in Figures S23–S25. These results indicate an intact crystal structure, unchanged morphology, and a small Au NCs size of 2.45 nm with a uniform distribution on the Cu/$TiO_2$ surface. The excellent stability of $Au_n$/Cu-$TiO_2$ may be due to the stronger interaction between Au NCs and Cu/$TiO_2$, inhibiting the photocorrosion and promoting the photoreduction reaction. The optimized design of $Au_n$/Cu-$TiO_2$ photocatalyst establishes a precise balance between the effective charge transfer and structural stability.

## 3 | Conclusion

In summary, we successfully synthesized an $Au_n$/Cu-$TiO_2$ photocatalyst where both photocatalytic activity and stability were greatly improved in $H_2$ production as compared to that of $TiO_2$ and Cu/$TiO_2$ as a result of the functional synergy between Au NCs and Cu SAs. The critical role of Cu SAs in fine-tuning the local environment and electron density in $Au_n$/Cu-$TiO_2$ photocatalyst was explored by comparing the properties of Au/$TiO_2$. Current experimental results and theoretical calculations indicate that the electrons transfer from $TiO_2$ to $Cu^{2+}$, reducing the latter species to $Cu^+$, followed by electron transport to Au NCs, where $H_2$ evolution takes place. Consequently, enhanced interfacial interaction was critical for the improved sintering resistance and corrosion stability of Au NCs. As a result, the optimal catalyst $Au_n$/Cu-$TiO_2$ demonstrates a high photocatalytic activity in $H_2$ production (16.67 $mmol \cdot g^{-1} \cdot h^{-1}$), which was 2, 4, 5, and 60 times higher than those of $Au_n$/Cu-$TiO_2$-uc, Cu/$TiO_2$, Au/$TiO_2$, and $TiO_2$, respectively. Meanwhile, the DFT calculation results further illustrated that Au NCs act as the active center with strong charge enrichment due to the presence of Cu SAs. This work provides a fundamental understanding for the rational design of an efficient solar-to-fuel conversion attractive photocatalyst.

## 4 | Experimental Section

### 4.1 | Synthesis of $Au_{25}(SR)_{18}$ Nanoclusters

$Au_{25}(SR)_{18}$ nanoclusters were synthesized using the method reported previously [78] and labeled as $Au_{25}$ NCs. The synthesized $Au_{25}$ NCs were analyzed by UV–vis spectroscopy (Figure S26). Three characteristic absorption peaks at around 400, 447 nm, and 683 nm confirmed the successful synthesis of $Au_{25}$ NCs [79, 80], which have a size of approximately 1.3 nm (Figure S27).

### 4.2 | Synthesis of $Au_n$/Cu-$TiO_2$ Photocatalyst

According to our previous reports [50, 81], the synthesized $NH_2$-MIL-125 was first dispersed in 50 mL $Cu(NO_3)_2$ aqueous solution with $Cu^{2+}$ concentration of 0.10 $mmol \cdot L^{-1}$ to form $Cu^{2+}$/$NH_2$-MIL-125 precursors, followed by calcination at 400°C in air for 5 h to obtain Cu-SAs/$TiO_2$. Then, $Au_{25}$ NCs were anchored on Cu-SAs/$TiO_2$ through electrostatic interaction. A prescribed quantity of $Au_{25}$ NCs (e.g., 0.7 mg, corresponding to 0.5 wt% Au loading) was dispersed in dichloromethane. Subsequently, 100 mg Cu-SAs/$TiO_2$ was introduced into the solution, and the mixture was stirred for 12 h at room temperature. The solid product was isolated by centrifugation, washed, and dried at 60°C. Finally, the

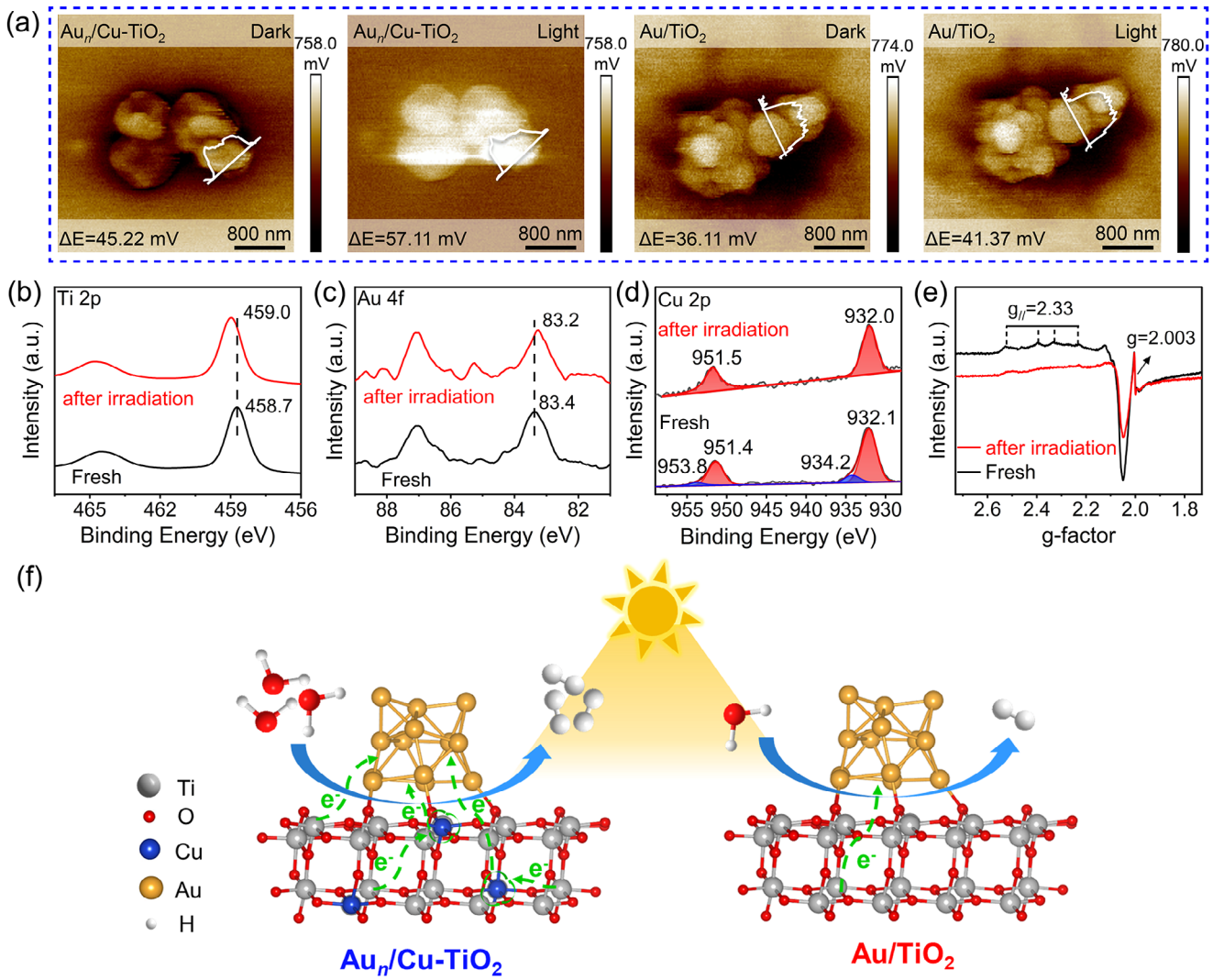


**FIGURE 6** | (a) The surface charge potential of $Au_n/Cu\text{-}TiO_2$ and $Au/TiO_2$. (b) XPS spectra of Ti 2p. (c) XPS spectra of Au 4f. (d) XPS spectra of Cu 2p. (e) Low temperature EPR spectra of $Au_n/Cu\text{-}TiO_2$. (f) Comparative photocatalytic hydrogen evolution mechanism for $Au_n/Cu\text{-}TiO_2$ and $Au/TiO_2$.

obtained powder was calcined at 400°C in air for 1 h to remove the thiolate ligand. The uncalcined catalyst with thiolate ligand was used for comparison and designated as $Au_n/Cu\text{-}TiO_2$-uc (where uc stands for the uncalcined catalyst).

### 4.3 | Synthesis of $Au/TiO_2$ and $Au/Cu\text{-}TiO_2$-PD Photocatalyst

To prepare the $Au/TiO_2$ catalyst, a similar preparation process to that of $Au_n/Cu\text{-}TiO_2$ photocatalyst was used, where the synthesis was carried out in the absence of any Cu precursors, leading to the formation of $Au/TiO_2$ catalyst. Photodeposited comparative sample ($Au/Cu\text{-}TiO_2$-PD) was prepared according to a previously reported method [82]. 100 mg of Cu-SAs/$TiO_2$ powder was added to 50 mL deionized water, mixed well, and then 154 μL $HAuCl_4 \cdot H_2O$ (5 mg·mL$^{-1}$) was added, illuminated under Xe light (13.30 W·m$^{-2}$) for 45 min. The powder was then collected by centrifugation and washed twice with deionized water and ethanol, respectively. Finally, the resulting powder was dried at 60°C for 12 h in air to obtain $Au/Cu\text{-}TiO_2$-PD.


#### Funding

This work was financially supported by the National Natural Science Foundation of China (52261135636, 12504314, and 21703001), Key Project of Anhui Province Department of Education (2022AH040076 and 2023AH050871), and the fund of the State Key Laboratory of Catalysis in DICP (N-22-12). E.O. and S.K. acknowledge financial support from The Scientific and Technological Research Council of Turkey (TÜBİTAK, Project Code: 122N441).


#### Conflicts of Interest

The authors declare no conflict of interest.

#### Data Availability Statement

The data that support the findings of this study are available from the corresponding author upon reasonable request.

#### References


1. L. Cao, Q. Luo, W. Liu, et al., "Identification of Single-Atom Active Sites in Carbon-Based Cobalt Catalysts during Electrocatalytic Hydrogen

Evolution," *Nature Catalysis* 2, no. 2 (2019): 134–141, https://doi.org/10.1038/s41929-018-0203-5.

2. Y. Wang, A. Vogel, M. Sachs, et al., "Current Understanding and Challenges of Solar-Driven Hydrogen Generation Using Polymeric Photocatalysts," *Nature Energy* 4, no. 9 (2019): 746–760, https://doi.org/10.1038/s41560-019-0456-5.

3. Y. Zhao, H. Zhou, X. Zhu, et al., "Simultaneous Oxidative and Reductive Reactions in One System by Atomic Design," *Nature Catalysis* 4, no. 2 (2021): 134–143, https://doi.org/10.1038/s41929-020-00563-0.

4. S. J. Moniz, S. A. Shevlin, D. J. Martin, Z.-X. Guo, and J. Tang, "Visible-Light Driven Heterojunction Photocatalysts for Water Splitting – A Critical Review," *Energy & Environmental Science* 8, no. 3 (2015): 731–759, https://doi.org/10.1039/c4ee03271c.

5. B.-H. Lee, S. Park, M. Kim, et al., "Reversible and Cooperative Photoactivation of Single-Atom Cu/$TiO_2$ Photocatalysts," *Nature Materials* 18, no. 6 (2019): 620–626, https://doi.org/10.1038/s41563-019-0344-1.

6. J. Tang, J. R. Durrant, and D. R. Klug, "Mechanism of Photocatalytic Water Splitting in $TiO_2$. Reaction of Water with Photoholes, Importance of Charge Carrier Dynamics, and Evidence for Four-Hole Chemistry," *Journal of the American Chemical Society* 130, no. 42 (2008): 13885–13891, https://doi.org/10.1021/ja8034637.

7. H. Yin, J. Yuan, J. Wang, S. Hu, P. Wang, and H. Xie, "Crystalline Nitrogen-Doped-Carbon Anchored Well-Dispersed $Fe_3O_4$ Nanoparticles for Real-Time Scalable Neutral $H_2O_2$ Electrosynthesis," *Energy & Environmental Science* 18, no. 5 (2025): 2231–2242, https://doi.org/10.1039/D4EE05796A.

8. R. Pan, X. Ge, Q. Liu, et al., "Synergic Delocalized-Conjugate and Electron-Deficient Effect and Mesoporous Channel Promote Photocatalytic Coupling $H_2$ Evolution with Benzyl-Alcohol Oxidation," *Advanced Functional Materials* 34, no. 17 (2024): 2315212, https://doi.org/10.1002/adfm.202315212.

9. A. L. Linsebigler, G. Lu, and J. T. Yates Jr, "Photocatalysis on $TiO_2$ Surfaces: Principles, Mechanisms, and Selected Results," *Chemical Reviews* 95, no. 3 (1995): 735–758, https://doi.org/10.1021/cr00035a013.

10. Y. Sun, J. Li, Z. Wang, and H. Zhu, "Au Nanostars/$Bi_2S_3$/$TiO_2$ Schottky/S-scheme Dual Heterojunctions for Efficient Photocatalytic Hydrogen Evolution," *Journal of Materials Chemistry A* 13, no. 36 (2025): 30457–30466, https://doi.org/10.1039/D5TA03337C.

11. X. Kang, H. Chong, and M. Zhu, "$Au_{25}(SR)_{18}$: the Captain of the Great Nanocluster Ship," *Nanoscale* 10, no. 23 (2018): 10758–10834, https://doi.org/10.1039/C8NR02973C.

12. T. U. Oguchi, Y. Ishii, and M. Ogawa, "Onset of Catalytic Activity of Gold Clusters on Titania with the Appearance of Nonmetallic Properties," *Science* 281, no. 5383 (1998): 1647–1650, https://doi.org/10.1126/science.281.5383.1647.

13. J. Peng, P. Wang, B. Wang, et al., "Exploration of Formation and Size-Evolution Pathways of Thiolate-Gold Nanoclusters in the CO-Directed $[Au_{25}(SR)_{18}]$ − Synthesis," *Small* 17, no. 27 (2021): 2000627, https://doi.org/10.1002/smll.202000627.

14. Y. Yu, Z. Luo, Y. Yu, J. Y. Lee, and J. Xie, "Observation of Cluster Size Growth in CO-Directed Synthesis of $Au_{25}(SR)_{18}$ Nanoclusters," *ACS Nano* 6, no. 9 (2012): 7920–7927, https://doi.org/10.1021/nn3023206.

15. G. Li, D.-E. Jiang, S. Kumar, Y. Chen, and R. Jin, "Size Dependence of Atomically Precise Gold Nanoclusters in Chemoselective Hydrogenation and Active Site Structure," *ACS Catalysis* 4, no. 8 (2014): 2463–2469, https://doi.org/10.1021/cs500533h.

16. M. S. Bootharaju, C. W. Lee, G. Deng, et al., "Atom-Precise Heteroatom Core-Tailoring of Nanoclusters for Enhanced Solar Hydrogen Generation," *Advanced Materials* 35, no. 18 (2023): 2207765, https://doi.org/10.1002/adma.202207765.

17. B. Weng, K.-Q. Lu, Z. Tang, H. M. Chen, and Y.-J. Xu, "Stabilizing Ultrasmall Au Clusters for Enhanced Photoredox Catalysis," *Nature Communications* 9, no. 1 (2018): 1543, https://doi.org/10.1038/s41467-018-04020-2.

18. H. Xie, J. Zhang, G. Xiao, and F.-X. Xiao, "Photosensitization of Transition Metal Chalcogenide with Metal Nanoclusters for Boosted Photocatalysis," *Molecular Catalysis* 581 (2025): 115149, https://doi.org/10.1016/j.mcat.2025.115149.

19. X.-H. Liu, Y. He, Z. Li, et al., "Size Transformation of Au Nanoclusters for Enhanced Photocatalytic Hydrogen Generation: Interaction Behavior at Nanocluster/Semiconductor Interface," *Journal of Colloid and Interface Science* 651 (2023): 368–375, https://doi.org/10.1016/j.jcis.2023.08.001.

20. B.-X. Zheng, J.-N. Yuan, P. Su, et al., "Alloy Nanocluster Artificial Photosystems Steering Photoredox Organic Transformation," *Journal of Materials Chemistry A* 13, no. 7 (2025): 4908–4920, https://doi.org/10.1039/d4ta08327j.

21. S. Chen, M. Li, S. Yu, et al., "Ligand Removal of $Au_{25}$ Nanoclusters by Thermal and Electrochemical Treatments for Selective $CO_2$ Electroreduction to CO," *The Journal of Chemical Physics* 155, no. 5 (2021), https://doi.org/10.1063/5.0059363.

22. A. Shivhare, D. M. Chevrier, R. W. Purves, and R. W. Scott, "Following the Thermal Activation of $Au_{25}(SR)_{18}$ Clusters for Catalysis by X-ray Absorption Spectroscopy," *The Journal of Physical Chemistry C* 117, no. 39 (2013): 20007–20016, https://doi.org/10.1021/jp4063687.

23. L. Luo and R. Jin, "Atomically Precise Metal Nanoclusters Meet Metal-Organic Frameworks," *Iscience* 24, no. 10 (2021): 103206, https://doi.org/10.1016/j.isci.2021.103206.

24. M. A. Abbas, T.-Y. Kim, S. U. Lee, Y. S. Kang, and J. H. Bang, "Exploring Interfacial Events in Gold-Nanocluster-Sensitized Solar Cells: Insights into the Effects of the Cluster Size and Electrolyte on Solar Cell Performance," *Journal of the American Chemical Society* 138, no. 1 (2016): 390–401, https://doi.org/10.1021/jacs.5b11174.

25. Z. Luo, X. Yuan, Y. Yu, et al., "From Aggregation-Induced Emission of Au(I)–Thiolate Complexes to Ultrabright Au(0)@Au(I)–Thiolate Core–Shell Nanoclusters," *Journal of the American Chemical Society* 134, no. 40 (2012): 16662–16670, https://doi.org/10.1021/ja306199p.

26. P. Haider, A. Urakawa, E. Schmidt, and A. Baiker, "Selective Blocking of Active Sites on Supported Gold Catalysts by Adsorbed Thiols and Its Effect on the Catalytic Behavior: a Combined Experimental and Theoretical Study," *Journal of Molecular Catalysis A: Chemical* 305, no. 1–2 (2009): 161–169, https://doi.org/10.1016/j.molcata.2009.02.025.

27. H. Chen, C. Liu, M. Wang, et al., "Visible Light Gold Nanocluster Photocatalyst: Selective Aerobic Oxidation of Amines to Imines," *ACS Catalysis* 7, no. 5 (2017): 3632–3638, https://doi.org/10.1021/acscatal.6b03509.

28. C. G. Long, J. D. Gilbertson, G. Vijayaraghavan, K. J. Stevenson, C. J. Pursell, and B. D. Chandler, "Kinetic Evaluation of Highly Active Supported Gold Catalysts Prepared from Monolayer-Protected Clusters: an Experimental Michaelis–Menten Approach for Determining the Oxygen Binding Constant during CO Oxidation Catalysis," *Journal of the American Chemical Society* 130, no. 31 (2008): 10103–10115, https://doi.org/10.1021/ja801279a.

29. S. Gaur, H. Wu, G. G. Stanley, K. More, C. S. S. R. Kumar, and J. J. Spivey, "CO Oxidation Studies over Cluster-Derived Au/$TiO_2$ and AUROlite Au/$TiO_2$ Catalysts Using DRIFTS," *Catalysis Today* 208 (2013): 72–81, https://doi.org/10.1016/j.cattod.2012.10.029.

30. D. A. Bulushev, V. I. Sobolev, L. V. Pirutko, et al., "Hydrogen Production from Formic Acid over Au Catalysts Supported on Carbon: Comparison with Au Catalysts Supported on $SiO_2$ and $Al_2O_3$," *Catalysts* 9, no. 4 (2019): 376, https://doi.org/10.3390/catal9040376.

31. L. Sun, X. He, Y. Yuan, et al., "Tuning Interfacial Sequence between Nitrogen-Doped Carbon Layer and Au Nanoparticles on Metal-Organic Framework-Derived $TiO_2$ to Enhance Photocatalytic Hydrogen Production," *Chemical Engineering Journal* 397 (2020): 125468, https://doi.org/10.1016/j.cej.2020.125468.

32. M. Torras, P. Molet, L. Soler, J. Llorca, A. Roig, and A. Mihi, "Au/$TiO_2$ 2D-Photonic Crystals as UV–Visible Photocatalysts for $H_2$ Production," *Advanced Energy Materials* 12, no. 6 (2022): 2103733, https://doi.org/10.1002/aenm.202103733.

33. B. Vedhanarayanan, C.-C. Chen, and T.-W. Lin, "Plasmon-Enhanced Photocatalytic Hydrogen Production by Dual Dye Sensitized Ternary Composite of $MoS_3$/Au Core-Ag Shell Nanoparticles/Graphene," *Journal of Power Sources* 477 (2020): 229033, https://doi.org/10.1016/j.jpowsour.2020.229033.

34. Y. Li, K. Huang, W. Liu, et al., "Interfacial Engineering of Carbon Quantum Dot/Metal-Organic Framework Heterostructures for Boosted Urea Electrosynthesis from Carbon Dioxide and Nitrate," *Journal of Colloid and Interface Science* 703 (2025): 139264, https://doi.org/10.1016/j.jcis.2025.139264.

35. X. Liu, H. Zhuang, J. Huang, et al., "Engineering $TiO_2$ Nanosheets with Exposed (001) Facets via the Incorporation of Au Clusters for Boosted Photocatalytic Hydrogen Production," *Materials Advances* 1, no. 6 (2020): 1608–1612, https://doi.org/10.1039/d0ma00479k.

36. M. Ge, Q. Li, C. Cao, et al., "One-Dimensional $TiO_2$ Nanotube Photocatalysts for Solar Water Splitting," *Advanced Science* 4, no. 1 (2017): 1600152, https://doi.org/10.1002/advs.201600152.

37. S. M. Wu and P. Schmuki, "Single Atom Cocatalysts in Photocatalysis," *Advanced Materials* 37, no. 7 (2025): 2414889, https://doi.org/10.1002/adma.202414889.

38. Y. Zhang, J. Zhao, H. Wang, et al., "Single-Atom Cu Anchored Catalysts for Photocatalytic Renewable $H_2$ Production with a Quantum Efficiency of 56%," *Nature Communications* 13, no. 1 (2022): 58, https://doi.org/10.1038/s41467-021-27698-3.

39. H. Wang, H. Qi, X. Sun, et al., "High Quantum Efficiency of Hydrogen Production from Methanol Aqueous Solution with PtCu–$TiO_2$ Photocatalysts," *Nature Materials* 22, no. 5 (2023): 619–626, https://doi.org/10.1038/s41563-023-01519-y.

40. T. Wang, F. Sun, S. Liu, G. Zhuang, and B. Li, "Dioxygen-Enhanced $CO_2$ Photoreduction on $TiO_2$ Supported Cu Single-Atom Sites," *Applied Catalysis B: Environmental* 325 (2023): 122339, https://doi.org/10.1016/j.apcatb.2022.122339.

41. X. Tao, R. Long, D. Wu, et al., "Anchoring Positively Charged Pd Single Atoms in Ordered Porous Ceria to Boost Catalytic Activity and Stability in Suzuki Coupling Reactions," *Small* 16, no. 43 (2020), https://doi.org/10.1002/smll.202001782.

42. B. Xiao, C. Shen, Z. Luo, et al., "Cu Surface Doped $TiO_2$: Constructing Cu Single-Atoms Active Sites and Broadening the Photo-Response Range for Efficient Photocatalytic Hydrogen Production," *Chemical Engineering Journal* 468 (2023): 143650, https://doi.org/10.1016/j.cej.2023.143650.

43. Y. Ma, Y. Zhang, Y. Ma, et al., "In Situ Cu Single Atoms Anchoring on MOF-Derived Porous $TiO_2$ for the Efficient Separation of Photon-Generated Carriers and Photocatalytic $H_2$ Evolution," *Nanoscale* 14, no. 42 (2022): 15889–15896, https://doi.org/10.1039/d2nr05099d.

44. R. Li, C.-W. Tung, B. Zhu, et al., "d-Band Center Engineering of Single Cu Atom and Atomic Ni Clusters for Enhancing Electrochemical $CO_2$ Reduction to CO," *Journal of Colloid and Interface Science* 674 (2024): 326–335, https://doi.org/10.1016/j.jcis.2024.06.176.

45. Y. Chen, S. Ji, W. Sun, et al., "Engineering the Atomic Interface with Single Platinum Atoms for Enhanced Photocatalytic Hydrogen-Production," *Angewandte Chemie International Edition* 59, no. 3 (2020): 1295–1301, https://doi.org/10.1002/anie.201912439.

46. Z. Wu, D.-E. Jiang, A. K. P. Mann, et al., "Thiolate Ligands as a Double-Edged Sword for CO Oxidation on $CeO_2$ Supported $Au_{25}(SCH_2CH_2Ph)_{18}$ Nanoclusters," *Journal of the American Chemical Society* 136, no. 16 (2014): 6111–6122, https://doi.org/10.1021/ja5018706.

47. R. Jin, X. Liu, S. Zhao, Y. Xing, and R. Jin, "Shape Effect of Atomically Precise $Au_{25}$ Nanoclusters on Catalytic CO Oxidation," *The Journal of Physical Chemistry C* 126, no. 40 (2022): 17114–17122, https://doi.org/10.1021/acs.jpcc.2c06066.

48. V. Sudheeshkumar, A. Shivhare, and R. W. Scott, "Synthesis of Sinter-Resistant Au@Silica Catalysts Derived from $Au_{25}$ Clusters," *Catalysis Science & Technology* 7, no. 1 (2017): 272–280, https://doi.org/10.1039/c6cy01822j.

49. J. Hong, X. Bai, X. Wang, et al., "Structural Factors of $Au_{25}$ Cluster as Precursor to Synthesize Au/$Nb_2O_5$ for Low-Temperature CO Oxidation," *Catalysis Today* 459 (2025): 115415, https://doi.org/10.1016/j.cattod.2025.115415.

50. R. Zhang, Y. Liu, C. Wang, et al., "Constructing Bifunctional $TiO_2$ from $NH_2$-MIL-125(Ti) for Excellent Photocatalytic Tetracycline Degradation," *Journal of Alloys and Compounds* 965 (2023): 171396, https://doi.org/10.1016/j.jallcom.2023.171396.

51. M. Tang, D. Yang, J. Wang, Q. Zhou, X. Zhu, and Y. Jiao, "Effects of Cu Doping on the Phase Transition and Photocatalytic Activity of Anatase/Rutile Mixed Crystal $TiO_2$ Nanocomposites," *Materials Research Express* 8, no. 8 (2021): 085007, https://doi.org/10.1088/2053-1591/ac1bcd.

52. Z. Liu, Y. Wu, J. Chen, et al., "Effective Elimination of As(III) via Simultaneous Photocatalytic Oxidation and Adsorption by a Bifunctional Cake-Like $TiO_2$ Derived from MIL-125(Ti)," *Catalysis Science & Technology* 8, no. 7 (2018): 1936–1944, https://doi.org/10.1039/c8cy00125a.

53. B. Zi, H. Zheng, T. Zhou, et al., "Changeable Active Sites by Pr Doping CuSA-$TiO_2$ Photocatalyst for Excellent Hydrogen Production," *Small* 20, no. 27 (2024): 2305779, https://doi.org/10.1002/smll.202305779.

54. P. Makula, M. Pacia, and W. Macyk, "How To Correctly Determine the Band Gap Energy of Modified Semiconductor Photocatalysts Based on UV–Vis Spectra," *The Journal of Physical Chemistry Letters* 9, no. 23 (2018): 6814–6817, https://doi.org/10.1021/acs.jpclett.8b02892.

55. P. R. Jubu, O. S. Obaseki, F. K. Yam, et al., "Influence of the Secondary Absorption and the Vertical Axis Scale of the Tauc's Plot on Optical Bandgap Energy," *Journal of Optics* 52, no. 3 (2022): 1426–1435, https://doi.org/10.1007/s12596-022-00961-6.

56. R. Pan, Y. Yang, C. Shi, G. Zou, J. Yuan, and H. Xie, "Symmetric C N Linkage Optimizing Electron Delocalization of Thiophene Ring over Crystalline Carbon Nitride for Efficient Photocatalytic $H_2O_2$ Production," *Journal of Colloid and Interface Science* 700, no. Pt 3 (2025): 138665, https://doi.org/10.1016/j.jcis.2025.138665.

57. Y. Chen, L. Soler, C. Xie, et al., "A Straightforward Method to Prepare Supported Au Clusters by Mechanochemistry and Its Application in Photocatalysis," *Applied Materials Today* 21 (2020): 100873, https://doi.org/10.1016/j.apmt.2020.100873.

58. Z. Wang, D. Brouri, S. Casale, L. Delannoy, and C. Louis, "Exploration of the Preparation of Cu/$TiO_2$ Catalysts by Deposition–Precipitation with Urea for Selective Hydrogenation of Unsaturated Hydrocarbons," *Journal of Catalysis* 340 (2016): 95–106, https://doi.org/10.1016/j.jcat.2016.05.011.

59. Y. Liu, Z. Wang, W. Wang, and W. Huang, "Engineering Highly Active $TiO_2$ Photocatalysts via the Surface-Phase Junction Strategy Employing a Titanate Nanotube Precursor," *Journal of Catalysis* 310 (2014): 16–23, https://doi.org/10.1016/j.jcat.2013.03.024.

60. Q. Zhang, Y. Chen, X. Yu, Y. Yin, Y. Ru, and G. Tian, "In Situ Construction of Schottky Junctions on MOF-Derived Defective $TiO_2$ Oval Nanocages for Enhanced Photocatalytic $CO_2$ Reduction," *Journal of Alloys and Compounds* 983 (2024): 173735, https://doi.org/10.1016/j.jallcom.2024.173735.

61. T. Zhou, T. Lv, B. Xiao, et al., "Cu and Pd Dual-Single-Atoms Anchored Titanium Dioxide for Remarkable Photocatalytic $H_2$ Evolution Efficiency," *Chemical Engineering Journal* 478 (2023): 147372, https://doi.org/10.1016/j.cej.2023.147372.

62. X. Jiang, Y. Bai, X. Wang, et al., "Bimetallic CuCo Nanoparticles Optimized Hydrogen Generation Active Centers Thereby Significantly Enhancing $TiO_2$ Photocatalytic Activity," *International Journal of Hydrogen Energy* 64 (2024): 120–131, https://doi.org/10.1016/j.ijhydene.2024.03.271.

63. X. Wang, J. Zhao, H. Eliasson, et al., "Very Low Temperature CO Oxidation over Atomically Precise Au 25 Nanoclusters on $MnO_2$," *Journal*

*of the American Chemical Society* 145, no. 50 (2023): 27273–27281, https://doi.org/10.1021/jacs.3c06372.

64. I. López-Hernández, V. Truttmann, C. Garcia, et al., "AgAu Nanoclusters Supported on Zeolites: Structural Dynamics during CO Oxidation," *Catalysis Today* 384-386 (2022): 166–176, https://doi.org/10.1016/j.cattod.2021.04.016.

65. T. Wang, X. Tao, X. Li, K. Zhang, S. Liu, and B. Li, "Synergistic Pd Single Atoms, Clusters, and Oxygen Vacancies on $TiO_2$ for Photocatalytic Hydrogen Evolution Coupled with Selective Organic Oxidation," *Small* 17, no. 2 (2021), https://doi.org/10.1002/smll.202006255.

66. S. Neubert, D. Mitoraj, S. A. Shevlin, et al., "Highly Efficient Rutile $TiO_2$ Photocatalysts with Single Cu(II) and Fe(III) Surface Catalytic Sites," *Journal of Materials Chemistry A* 4, no. 8 (2016): 3127–3138, https://doi.org/10.1039/c5ta07036h.

67. P. Chen, Z. Li, P. Wang, et al., "Synergistic Effect of Atomically Dispersed Cu Species and Ti-Defects for Boosting Photocatalytic $CO_2$ Reduction over Hierarchical $TiO_2$," *Nanoscale* 16, no. 22 (2024): 10727–10736, https://doi.org/10.1039/d4nr01229a.

68. Y. Zhang, J.-X. Liu, K. Qian, et al., "Structure Sensitivity of Au-$TiO_2$ Strong Metal–Support Interactions," *Angewandte Chemie International Edition* 60, no. 21 (2021): 12074–12081, https://doi.org/10.1002/anie.202101928.

69. W. Wang, C. Deng, S. Xie, et al., "Photocatalytic C–C Coupling from Carbon Dioxide Reduction on Copper Oxide with Mixed-Valence Copper(I)/Copper(II)," *Journal of the American Chemical Society* 143, no. 7 (2021): 2984–2993, https://doi.org/10.1021/jacs.1c00206.

70. H. Wang, X. Liu, W. Yang, et al., "Surface-Clean Au 25 Nanoclusters in Modulated Microenvironment Enabled by Metal–Organic Frameworks for Enhanced Catalysis," *Journal of the American Chemical Society* 144, no. 48 (2022): 22008–22017, https://doi.org/10.1021/jacs.2c09136.

71. Y. Yu, X. Dong, P. Chen, et al., "Synergistic Effect of Cu Single Atoms and Au–Cu Alloy Nanoparticles on $TiO_2$ for Efficient $CO_2$ Photoreduction," *ACS Nano* 15, no. 9 (2021): 14453–14464, https://doi.org/10.1021/acsnano.1c03961.

72. K. Yan, X. Ge, Y. Cao, et al., "Pd Ensemble Sites Tuned Local Environment of Cu Catalysts for Matching Propyne Semi-Hydrogenation," *Angewandte Chemie International Edition* 64, no. 19 (2025): 202503263, https://doi.org/10.1002/anie.202503263.

73. D. Tan, T. Ding, K. Shen, et al., "Icosahedron Kernel Defect in $Pt_1Ag_x$ Series of Bimetallic Nanoclusters Enhances Photocatalytic Hydrogen Evolution," *Chemical Science* 16, no. 21 (2025): 9326–9336, https://doi.org/10.1039/d5sc01735a.

74. Y. Li, B. Wei, M. Zhu, et al., "Synergistic Effect of Atomically Dispersed Ni–Zn Pair Sites for Enhanced $CO_2$ Electroreduction," *Advanced Materials* 33, no. 41 (2021): 2102212, https://doi.org/10.1002/adma.202102212.

75. Z. Fan, Q. Xu, Y. Wang, et al., "Electron Regulation Accelerates Photocatalytic Hydrogen Evolution for Bimetallic Pt, Au on CdS Nanorods," *Chemical Engineering Journal* 511 (2025): 162016, https://doi.org/10.1016/j.cej.2025.162016.

76. R. Pan, J. Yuan, X. Huang, Q. Liu, Y. Cui, and B. Wu, "Engineering Conjugated Tetrone-Imide-Linked Tubular Carbon Nitride for Boosting Kinetics of Overall Water Splitting," *Advanced Functional Materials* (2025), https://doi.org/10.1002/adfm.202513118.

77. R. Pan, W. Lv, X. Ge, et al., "Electron-Deficient Engineering in Large-Conjugate-Heptazine Framework to Effectively Shuttle Hot Electrons for Efficient Photocatalytic $H_2O_2$ Production," *Advanced Functional Materials* 35, no. 4 (2025): 2414193, https://doi.org/10.1002/adfm.202414193.

78. T. Phongamwong, N. Barrabés, W. Donphai, T. Witoon, G. Rupprechter, and M. Chareonpanich, "Chlorophyll-Modified $Au_{25}(SR)_{18}$-Functionalized $TiO_2$ for Photocatalytic Degradation of Rhodamine B," *Applied Catalysis B: Environmental* 325 (2023): 122336, https://doi.org/10.1016/j.apcatb.2022.122336.

79. Z. Liu, Y. Li, E. Kahng, et al., "Tailoring the Electron–Phonon Interaction in Au 25 (SR) 18 Nanoclusters via Ligand Engineering and Insight into Luminescence," *ACS Nano* 16, no. 11 (2022): 18448–18458, https://doi.org/10.1021/acsnano.2c06586.

80. C. Yu, G. Li, S. Kumar, H. Kawasaki, and R. Jin, "Stable $Au_{25}(SR)_{18}/TiO_2$ Composite Nanostructure with Enhanced Visible Light Photocatalytic Activity," *The Journal of Physical Chemistry Letters* 4, no. 17 (2013): 2847–2852, https://doi.org/10.1021/jz401447w.

81. R. Zhang, W. Zhang, Q. Zhu, et al., "Engineering Polydopamine-Functionalized $NH_2$-MIL-125(Ti) for Tetracycline Degradation and Antibacterial Applications," *Surfaces and Interfaces* 54 (2024): 105188, https://doi.org/10.1016/j.surfin.2024.105188.

82. S. F. Chen, J. P. Li, K. Qian, et al., "Large Scale Photochemical Synthesis of M@$TiO_2$ Nanocomposites (M = Ag, Pd, Au, Pt) and Their Optical Properties, CO Oxidation Performance, and Antibacterial Effect," *Nano Research* 3, no. 4 (2010): 244–255, https://doi.org/10.1007/s12274-010-1027-z.

## Supporting Information

Additional supporting information can be found online in the Supporting Information section.

**Supporting File**: adfm74432-sup-0001-SuppMat.docx.